Liang Zhang[1], Xubing Zhang[2], Maosheng Yang[1], Xiao Xiao[1], Denggao Qiu[3], Jianguo Yan[3], Long Xiao[1], and Jun Huang[1,4]

[1]State Key Laboratory of planetary processes and mineral resources, School of Earth Sciences, China University of Geosciences (Wuhan), Wuhan 430074, China

[2]School of Geography and Information Engineering, China University of Geosciences, Wuhan 430078, China

[3]State Key Laboratory of Information Engineering in Surveying, Mapping and Remote Sensing, Wuhan University, Wuhan 430070, China

[4]Chinese Academy of Sciences Center for Excellence in Comparative Planetology, Hefei 230026, China

Corresponding author: Jun Huang(junhuang@cug.edu.cn)

Key Points:

- By introducing the CE-5 sample point data, the previous lunar sample point data are enriched and supplemented
- Based on the MI multispectral data and 1D-CNN model, new distribution maps of five oxides and Mg # are generated
- We present regions of mare domes, and irregular mare patches (IMPs) to demonstrate the composition variations and geologic implications of these new maps.

Abstract

In the past, global maps of major oxides and Mg # of the lunar surface had been derived from spectral data with "ground truth" geochemical information from Apollo and Luna samples. These compositional maps provide insights into the chemical variations of different geologic units, thus the regional and global geologic evolution. In this study, we produced new global maps of major oxides (Al_2O_3, CaO, FeO, MgO, and TiO_2) and Mg # with imaging spectral data of KAGUYA multiband imager (MI) with the one dimensional-convolutional neural network 1D-CNN algorithm, taking advantage of recently acquired geochemical information of China's Chang'E-5 (CE-5) samples. The coefficients of determination (R^2) and Root Mean Squared Error (RMSE) were selected as the model evaluation indicators, and compared with the models used by Wang et al. (2021) and Xia et al. (2019), the results showed that the 1D-CNN algorithm model used in this study had a higher degree of fit and smaller dispersion between the ground true value and the predicted value. The 1D-CNN algorithm generally performs better in describing the complex nonlinear relationship between spectra and chemical components. In addition, we present regions of mare domes in Mairan Dome (43.76°N, 49.90°W), and irregular mare patches (IMPs) in Sosigenes (8.34°N, 19.07°E) to demonstrate the geologic implications of these new maps. With the highest spatial resolution (~ 59 m / pixel), these new maps

of major oxides and Mg # will serve as an important guide in the future study of lunar geology.

Plain Language Summary

The moon is composed of many elements and oxides. The compositional maps of major oxides and Mg # of the lunar surface provide insights into the chemical variations of different geologic units, thus the regional and global geologic evolution. In this study, we produced new global maps of major oxides (Al_2O_3, CaO, FeO, MgO, and TiO_2) and Mg # with imaging spectral data of KAGUYA multiband imager (MI) with the one dimensional-convolutional neural network 1D-CNN algorithm, taking advantage of recently acquired geochemical information of China's Chang'E-5 (CE-5) samples. These results have high inversion accuracy and a high spatial resolution of 59 m / pixel. In addition, we present regions of mare domes in Mairan Dome (43.76°N, 49.90°W), and irregular mare patches (IMPs) in Sosigenes (8.34°N, 19.07°E) to demonstrate the composition variations and geologic implications of these new maps.

1 Introduction

The study of the major oxides (e.g., Al_2O_3, CaO, FeO, MgO, and TiO_2) and Mg # (molar or atomic ratio of Mg / [Mg + Fe]) of the lunar surface is of great significance for understanding the geologic evolution of the moon. Among them, iron is one of the most abundant elements in lunar silicate minerals (Wilcox et al., 2005). Titanium is used in mare basalt classification (e.g., Charette et al., 1974; Taylor et al., 1991; Giguere et al., 2000). The study of iron and titanium elements is important for the recognition of mineralogy and crustal evolution of the moon (Taylor, 1987; Lucey et al., 1995, 2000a; Ling et al., 2010, 2011; Sun et al., 2016). In addition, the distribution of iron and titanium on the lunar surface is also of great significance to the development and utilization of lunar resources (Heiken et al., 1991). Besides the elements of iron and titanium, the elements of aluminum, calcium, and magnesium are also major chemical compositions in lunar rock (Papike, 1988). Mg # is related to the source region, composition, partial melting degree of primitive magma, and the evolution process of magma (Taylor et al., 2006).

Various studies have shown correlations between spectra and the abundance of major oxide elements on the moon surface (Haggerty, 1972; Adams and Charette, 1975; Hapke et al., 1975; Liebermann and Ringwood, 1976; Pieters et al., 2000). Major oxides maps have been produced with Lunar Reconnaissance Orbiter Camera (LROC) Wide Angle Camera (WAC) Ultraviolet-Visible (UV-VIS) data (Sato et al., 2017), China's Chang'E-1 (CE-1) Interference Imaging Spectrometer (IIM) data (Wu, 2012; Yan et al., 2012; Sun et al., 2016; Xia et al., 2019), Clementine UV-VIS data (Lucey et al., 1995, 2000a; Gillis et al., 2003, 2004), The Moon Mineralogy Mapper (M^3) data (Bhatt et al., 2020; Surkov et al., 2020) and KAGUYA Multiband Imager (MI) data (Otake et al., 2012; Lemelin et al., 2015, 2016; Qiu et al., 2021; Wang et al., 2021). The FeO and TiO_2 abundances were calculated with linear inversion models constructed with spectral band

ratios (Lucey et al., 1995, 2000a; Otake et al., 2012; Wu et al., 2012; Yan et al.,2012). Other oxides (e.g., Al_2O_3, CaO and MgO) abundances have been derived with non-linear inversion models, including the partial least squares regression (PLSR) model (Wu 2012; Sun et al., 2016), neural networks (NN) model (Xia et al., 2019), support vector machine (SVM) model (Bhatt et al., 2020; Wang et al., 2021), random forest (RF) model (Qiu et al., 2021)and other machine learning algorithm models (Zhuang et al., 2020; Vulova et al., 2021).

Geochemical data of the returned lunar samples and in situ measurements are bench marks of the oxide maps derived from orbital reflectance spectral data. The samples used in previous studies include the Apollo and Luna samples and the Alpha Particle X-ray spectrometer (APXS) data (Fu et al., 2014) of the Chang'E-3 (CE-3) Yutu rover at northern Imbrium. In December 2020, China's Chang'E-5 (CE-5) mission returned 1.731kg samples from the northern Oceanus Procellarum (43.06°N, 51.92°W). These samples are mostly derived from local basalt (Qian et al., 2021a, 2021b; Jia et al., 2021, 2022), which erupted ~ 2 Ga ago (Che et al., 2021; Li et al., 2021), thus the youngest samples returned. The addition of the new sample data of CE-5 is of great value for the update of lunar surface oxide abundance maps.

The one dimensional-convolutional neural network (1D-CNN) model is a non-linear inversion model, which is demonstrated better (Chen et al., 2016; Malek et al., 2018; Qiu et al., 2021) in learning the relevant information between spectra as features from the spectral data than linear models and other machine learning models (e.g., random forest algorithm). The KAGUYA MI of preprocessing is a lunar imaging spectrometer with the highest spatial resolution (~ 59 m / pixel) (Ohtake et al., 2013). With the MI global mosaic and the additional geochemical information from CE-5 samples, we use 1D-CNN algorithm to build an optimized spectral inversion model, and generate lunar surface abundance maps of five major oxides (Al_2O_3, CaO, MgO, FeO, and TiO_2) and Mg #. We have also selected several regions to demonstrate the usage of these new maps.

2 Data and Methods

2.1 Data

The MI data includes 9 spectral bands, of which the UV-VIS band centers are 415, 750, 900, 950, and 1001 nm, and the NIR band centers are 1000, 1050, 1250, and 1550 nm. The global mosaic covers the range from 65°N ~ 65°S on the lunar surface (Ohtake et al., 2008), with a spatial resolution of ~ 59 m / pixel. We use eight bands (415, 750, 900, 950, 1001, 1050, 1250, and 1550 nm) of the MI global mosaic to calculate the abundances of the oxides.

For the bench mark points (Table 1), we included CE-5 samples (Tian et al., 2021; Li et al., 2022; Zong et al., 2022), Apollo samples (except for Apollo 11, whose sampling site is not covered by the MI global mosaic), Luna samples, and in situ measurements of CE-3 rover (Zhang et al., 2015; Ling et al., 2015). In order to reduce the noise impact of MI data, the reflectance of each bench

mark points by adopting the average reflectance value in the 2×2 or 3×2 pixels (Dataset S1).

2.2 Methods

2.2.1 Correlation coefficients between oxides and MI spectra

High Pearson correlation coefficients exist between MI spectra and oxide content (Figure 1), therefore, MI spectra can be used to retrieve the abundances of five oxides. In Figure 2, for each oxide, an MI wavelength (e.g., 1001nm, 1049nm, 1548nm) is used as an example to show the correlation between MI spectra and oxide content, in which univariate linear or polynomial regression models for some major oxides (such as CaO and FeO) can obtain good fitting results. However, some oxides (such as TiO_2) are difficult to calculate with traditional univariate regression models due to their complex relationship with the spectra. Therefore, we use the 1D-CNN algorithm to calculate the abundances of all five major oxides on the lunar surface.

2.2.2 The convolutional neural network model

As one of the representative deep learning algorithms, Convolutional neural network (CNN) was initially proposed to solve the problem of image recognition and classification (Lecun et al., 1998). In recent studies, CNN has been introduced in spectroscopy analysis to extract local abstract features of spectral data and establish end-to-end models between spectral data and target indicators and then used to solve regression problems (Malek et al., 2018; Chen et al., 2019; Qiu et al., 2021; Yuan et al., 2022). CNN belongs to the feedforward neural network, which is generally composed of convolution layers, activation functions, pooling layers, and fully connected layers.

In the convolution layer, the convolution kernel slides on the data signal to complete feature extraction, and then the nonlinear activation function is used to output the feature vector. The CNN activation function usually selects ReLU with faster calculation speed and convergence speed (Glorot et al., 2011). The formula for ReLU is as follows:

(1)

The convolution operation process is:

(2)

where y is the output result after weighted average of convolution layer; is the weight of the convolution kernel; b is the offset parameter.

After the convolution layer, there is a pooling layer, which is usually used to prevent information redundancy and overfitting. The fully connected layer is usually set before the network output layer, which is used to integrate the features extracted by multiple convolution layers and pooling layers, and obtain the target indicators.

Based on CNN, we use the 1D-CNN to construct a mathematical model to describe the relationship between the measured oxide content and the reflectivity of each sampling area (Dataset S1). 1D-CNN can avoid the extraction of information from other non-important elements, which can improve the learning efficiency of the network. Meanwhile, 1D-CNN adopts a weight-sharing mechanism, which can greatly reduce the number of parameters of the whole network, which is very important to improve the regression efficiency of the network. As shown in Figure 3, the 1D-CNN includes 4-layer convolution layer, 2-layer pooling layer and 1-layer full connection layer in this study. The input data corresponds to the spectral reflectance of 8 bands. The feature between bands is extracted by convolution. Then, the size of feature vectors is compressed by pooling to avoid overfitting. Next, feature vectors are extracted from the full connectivity layer. Finally, by using the linear activation function, the extracted features are transformed into the corresponding sample data (i.e., the measured value of oxide content).

2.2.3 Model tuning and evaluation measures

The proposed network was trained on the training and validation set to establish the calibration model. The mean square error was selected as the loss function of the regression model to detect the deviation between the predicted and measured values. During the training stage, the model weights were adjusted adaptively based on the Adam algorithm (Kinama & Ba, 2014) and the model batch size was set to 10. ReLU function was used as the activation function in the model. The initial learning rate was set as 0.001 and the maximum number of training iterations was set to 500 epochs. The model was implemented in Python using Keras framework (Ketkar, 2017).

The model performance was evaluated by the root mean squared error (RMSE), the coefficient of determination (R^2) in this work.

R^2 measures how well a statistical model predicts an outcome. The lowest possible value of R^2 is 0 and the highest possible value is 1. Put simply, the better a model is at making predictions, the closer its R^2 will be to 1. The formula for calculating R^2 is as follows:

(3)

where y represents predicted sampling point data; represents real sampling point data; represents the average value of real sampling point data.

RMSE is used to measure the deviation between the predicted value and the true value. The formula for calculating RMSE is as follows:

(4)

3 Results

3.1 Maps of the Major Elements and Mg #

The global maps of five major oxides and Mg # are shown in Figure 4. From a

global perspective, the five oxides exhibit dichotomous distributions between the highlands and the maria. For example, there is an obvious negative correlation between Al_2O_3, CaO and TiO_2, FeO, MgO in the maria. The least Al_2O_3 and CaO are present in the central regions of Oceanus Procellarum, Mare Imbrium, Tranquillitatis, and Serenitatis, but more in the boundary regions between the maria and highlands, while it is the opposite for TiO_2, FeO and MgO. In addition, ray materials of some craters (e.g., Tycho crater) are prominent in the maps of the major oxides, especially Al_2O_3 and CaO (Figure 4a and Figure 4b). We identify that the bottom and eastern parts of Tycho crater are elevated in Al_2O_3 and CaO. The global average Mg # is 0.675 is very close to the MI Mg # reported (0.67) by Wang et al. (2021), but higher than the CE-1 IIM-derived Mg # (0.644, Wu, 2012; 0.646, Xia et al., 2019), the Clementine optimized Mg # (0.57, Crites & Lucey, 2015), the LP GRS Mg # (0.606, Prettyman et al., 2006) and the Diviner Mg # (0.652, Ma et al., 2022). The average Mg # in maria is 0.527, while that of the highlands is 0.705. With the characteristics of the Mg #, we are able to distinguish the boundaries of three lunar crustal terranes (Figure 4f, red polyline, and blue polyline) including the Procellarum KREEP Terrane (PKT), The Feldspathic Highland Terrane (FHT) and the South Pole-Aitken Terrane (SPAT) proposed by Jolliff et al. (2000).

3.2 Comparison with previous work

The systematic differences in the average oxide abundances in the maria, highlands, and global (Table 2) are presented. The global abundance of Al_2O_3 and CaO in this study are 23.44 wt.% and 14.37 wt.%, Close to 23.56 wt.% and 14.20 wt.% proposed by Wang et al. (2021), Less than 25.32 wt.% and 16.89 wt.% proposed by Wu (2012). The global abundance of FeO and MgO in this study are 7.42 wt.% and 7.46 wt.%, Close to 7.40 wt.% and 7.67 wt.% of Wang et al. (2021), Higher than 6.42 wt.% and 6.46 wt.% of Wu (2012). The global abundance of TiO_2 in this study is 1.34 wt.%, Higher than 1.15 wt.% of Wang et al. (2021), Less than 1.54 wt.% of Wu (2012).

The histograms of the five oxide abundances and Mg # are shown in Figure 5, respectively. Except for TiO_2, which features a unimodal continuum distribution, all other elements exhibit bimodal distributions, excluding spike interference, corresponding to the maria and highlands respectively, generally consistent with previous studies on the distribution difference of major elements in the maria and highlands (Lucey et al., 1998; Gillis et al., 2004; Prettyman et al., 2006; Wu 2012; Lu et al. 2021). For example, the lower modal Fe abundance of ~ 4.12 FeO wt.% and the higher modal Fe abundance of ~ 18.23 FeO wt.%, which correspond to the highland areas and mare areas, respectively, are a little lower than the abundance of ~ 5.57 wt.% given by Wu (2012), close to the abundance of ~ 4.1 wt.% given by Wang et al. (2021), or ~ 4.7 wt.% and ~ 4.82 wt.% given by Prettyman et al.(2006) and Lucey et al. (1998).

4 Discussion

4.1 Model accuracy evaluation

The 1D-CNN model establishes a nonlinear regression model between the MI 8 band spectra and 40 sampling points by learning the data characteristics between the MI 8 band spectra and the true values of 40 sampling points, so that the major oxide abundance information of the sampling points can be retrieved based on the MI spectral data, and the data inversion results from 40 sampling points can be obtained. The effect of 1D-CNN model is evaluated by calculating R^2 and RMSE between 1D-CNN inversion data and laboratory truth data of 40 sampling points. See Table 3 and Figure 6 for inversion results and accuracy of five major oxides of 1D-CNN model.

The prediction accuracies of the 1D-CNN model for the five oxides are shown in Figure 6. All the R^2 are greater than 0.95 and greater than 0.99 for Al_2O_3, especially. To further illustrate the advantages of 1D-CNN model, a comparison of five major oxide abundances derived from this work with Wang et al. (2021) and Xia et al. (2019) is shown in Table 3. Compared with the inversion results of Wang et al. (2021), the 1D-CNN model in this study has higher R^2, and the regression model fitting effect is better; Compared with the results of Xia et al. (2019), their R^2 is equivalent, but the RMSE value of 1D-CNN model is lower, and the dispersion of the inversion data of regression model is lower. On the whole, compared with the former two models, the accuracy of this research model is relatively better.

On a global scale, we also compare the new maps of major oxides in this work and the maps of Wang et al. (2021) within the range 65°N ~ 65°. These maps are generally consistent (Figure S1).

4.2 Regional Analysis

We selected two compositionally interesting regions shown in this study (Figure 7; Figure S2), including Mairan Domes (43.76°N, 49.90°W) and Sosigenes (8.34°N, 19.07°E). Then, by analyzing the inversion results of five major oxides to demonstrate the geologic implications of these new maps.

4.2.1 Mairan Domes

Lunar mare domes are rounded to somewhat irregular convex landforms. They are characterized by a lower slope (generally less than 5°) and can reach a diameter of 30 km (Head & Gifford, 1980). Lunar mare domes can be divided into two different types. One type is mainly located in the center of the mare likely Marius Hills. The composition of these domes is similar to the background. The others are distributed near the highlands of the mare. Their composition is quite different from the surrounding mare basalt. Head & Gifford (1980) consider that the two types of domes are related to the interaction of lava deposits with preexisting topography by draping or kipuka formation and primary lava vent areas.

We analyzed Mairan Domes in this study (Figure 8). The Mairan Domes are a group of four domes at the northeast of Oceanus Procellarum near the highlands (Glotch et al., 2011). The four domes are Northeast Dome, Mairan T Dome,

Middle Dome, and South Dome from north to south, respectively. Five elements content of Mairan Domes are shown in Table 5. The four domes have a significant difference in composition with the surrounding mare. The domes have FeO abundances ranging from 9 – 13 wt.% FeO. This means that the domes were formed at a different time than the surrounding mare. The Northeast Dome has very close components to the highlands of the east. However, the other three domes also have some differences with the composition of the highlands, especially the Middle Dome. Although the Middle dome is partly bordered by the highlands, there are significant differences in the content of Al_2O_3. The Al_2O_3 contents of the three domes (Mairan T, Middle, and South) are higher than the highlands and Northeast Dome. This suggested that the origin of Northeast Dome may be different from the other three domes. Based on our model, the Al_2O_3 content of the units from high to low are the Mairan T Dome, South Dome, Middle Dome, Northeast Dome, highlands, and surrounding mare in the Mairan Domes region.

4.2.2 Sosigenes

IMPs are characterized by their young and small irregularly shaped depression composed of mounds and hummocky and blocky terrains (Qiao et al., 2020). Most of the IMPs are distributed in the mare unit from 3.9 to 3.1 billion years ago, suggesting that their origin may be related to the peak period of global lunar volcanism (Braden et al., 2014).

We analyzed Sosigenes in this study (Figure 9). Sosigenes (8.34°N, 19.07°E) was discovered on the Lunar Reconnaissance Orbiter Narrow Angle Camera (LROC NAC) image by Stooke (2012). Qiao et al. (2018) produced a Geologic sketch map of Sosigenes. The Sosigenes IMP floor can be categorized in terms of three morphologic units (Mound Units, Hummocky Units, and Blocky Units) (Qiao et al., 2018).

Five elements content of Sosigenes are shown in Table 6. Our oxide diagrams clearly distinguish the three units, indicating a huge difference in the oxide composition of the three units (Figure 9). Mound Units are characterized by high MgO, CaO, Al_2O_3 and low TiO_2 compared with the other two units likely surrounding mare. Hummocky Units have a similar oxide composition to Blocky Units, with the main difference being Al_2O_3. Hummocky Units have lower Al_2O_3 than Blocky Units.

5 Conclusions

This work complements the data of the CE-5 sampling point based on the previous sampling point data and reports the new map of five major oxides and Mg # on the moon of high spatial resolution (59 m / pixel). The 1D-CNN model, one of the deep learning algorithms, was selected as the method. The prediction results of the proposed model were compared with Xia et al. (2019) and Wang et al. (2021) models. The 1D-CNN model had higher R^2 ($R^2 \rightarrow 1$) and lower RMSE, which implied that it had a satisfactory generalization ability and high fitting degrees. It could make a good quantitative prediction of the

major oxide content on the lunar surface by establishing a linear and complex nonlinear relationship between chemical composition and spectral characteristics. By analyzing the major oxide content of lunar mare domes and IMPs in the study area, we found that the formation and lithology can be identified according to the oxide content. thus, the new oxide maps suggested in this work may provide clues for the identification of formation and lithology and further for lunar evolution.

Declaration of competing interest

The authors declare that they have no known competing financial interests or personal relationships that could have appeared to influence the work reported in this paper.

Data availability Statement

Data links are included in the acknowledgments.

Acknowledgments

The CE-1 DOM global mosaic is provided by China National Space Agency and the Science and Application Center for Moon and Deep Space Exploration, and accessible from plantes.cug.edu.cn. KAGUYA Multiband Imager maps are accessible from https://planetarymaps.usgs.gov/mosaic/Lunar_MI_multispectral_maps/ , and the Lunar Prospector GRS data are from https://pds-geosciences.wustl.edu/lunar/lp-l-grs-5-elem-abundance-v1/ . This study was supported by the National Natural Science Foundation of China (42273041) and Wuhan Science and Technology Plan Project-Application Basic Frontier Project (2019010701011403).

Open Research

All data are available within this article and its supplementary material. The Mg# values and the abundances of five major oxides: Al_2O_3, CaO, MgO, FeO and TiO_2 are available in the repository Zenodo via DOIs: https://doi.org/10.5281/zenodo.7262473, https://doi.org/10.5281/zenodo.7263324, https://doi.org/10.5281/zenodo.7263425, https://doi.org/10.5281/zenodo.7263592, https://doi.org/10.5281/zenodo.7264328, and https://doi.org/10.5281/zenodo.7264372.

References

Adams, J.B., & Charette, M.P. (1975). Spectral reflectance of highland rock types at Apollo 17: evidence from Boulder 1, station 2. *The Moon*, 14 (3–4), 483–489. https://doi.org/10.1007/BF00569678

Bhatt, M., et al. (2020). *A Comparison of elemental abundances derived from CHANDRAYAAN-2 Class and CHANDRAYAAN-1 M^3 from the Western Nearside of the Moon*. Paper presented at 51rd Lunar and Planetary Science Conference (abstract # 2270).

Braden, S.E., Stopar, J.D., Robinson, M.S., et al. (2014). Evidence for basaltic volcanism on the Moon within the past 100 million years. *Nature Geoscience*, 7(11), 787-791. https://doi.org/10.1038/ngeo2252

Charette, M.P., Mccord, T.B., Pieters, C.M., et al. (1974). Application of remote spectral reflectance measurements to lunar geology classification and determination of titanium content of lunar soils. *J. Geophys Res*, 79, 1605–1613. https://doi.org/10.1029/JB079i011p01605

Chen, X., He, X. Y., Zhou, G. X., Wang, B., Feng, G., Yu, H., & Ji, Y. (2019). Fast and accurate decoding of Raman spectra-encoded suspension arrays using deep learning. *Analyst*, 144 (14): 4312–4319. https://doi.org/10.1039/C9AN00913B

Che, X., Nemchin, A., Liu, D., et al. (2021). Age and composition of young basalts on the Moon, measured from samples returned by Chang'e-5. *Science* (New York, N.Y.), 374(6569), 887-890. https://doi.org/10.1126/science.abl7957

Chen, Y., Jiang, H., Li, C., Jia, X., & Ghamisi, P. (2016). Deep feature extraction and classification of hyperspectral images based on convolutional neural networks. *IEEE Trans. Geosci. Remote Sens*, 54, 6232–6251. https://doi.org/10.1109/TGRS.2016.2584107

Crites, S.T., & Lucey, P.G. (2015). Revised mineral and mg# maps of the moon from integrating results from the lunar prospector neutron and gamma-ray spectrometers with Clementine spectroscopy. *Am. Mineral*, 100 (4), 973–982. https://doi.org/10.2138/am-2015-4874

Fu, X. H., Li, C. L., Zhang, G. L., et al. (2014). Data processing for the Active Particle-induced X-ray Spectrometer and initial scientific results from Chang0e-3 mission. *Res. Astron. Astrophys*, 14, 1595–1606. https://doi.org/10.1088/1674–4527/14/12/008

Giguere, T.A., Taylor, G.J., Hawke, B.R., et al. (2000). The titanium contents of lunar mare basalts. *Meteoritics and Planetary Science*, 35 (1), 193-200. https://doi.org/10.1111/j.1945-5100.2000.tb01985.x

Gillis, J.J., Jolliff, B.L., & Elphic, R.C. (2003). A revised algorithm for calculating TiO_2 from Clementine UVVIS data: a synthesis of rock, soil, and remotely sensed TiO_2 concentrations. *J. Geophysical Res*, 108 (E2). https://doi.org/10.1029/2001JE001515

Gillis, J.J., Jolliff, B.L., & Korotev, R.L. (2004). Lunar surface geochemistry: global concentrations of Th, K, and FeO as derived from lunar prospector and Clementine data. *Geochem. Cosmochim. Acta*, 68 (18), 3791–3805. https://doi.org/10.1016/j.gca.2004.03.024

Glorot, X., Bordes, Y., & Bengio, Y. (2011). *Deep sparse rectifier neural networks*. Proceedings of the fourteenth international conference on artificial intelligence and statistics, JMLR Workshop and Conference Proceedings. pp. 315-323

Glotch, T.D., Hagerty, J.J., Lucey, P.G., et al. (2011). The Mairan domes: Silicic volcanic constructs on the Moon. *Geophysical Research Letters*, 38 (21). https://doi.org/10.1029/2011GL049548

Haggerty, S.E. (1972). Luna 16: an opaque mineral study and a systematic examination of compositional variations of spinels from Mare Fecunditatis. *Earth Planet. Sci. Lett*, 13 (2), 328–352. https://doi.org/10.1016/0012-821X(72)90109-4

Hapke, B., Cassidy, W., & Wells, E. (1975). Effects of vapor-phase deposition processes on the optical, chemical, and magnetic properties OE the lunar regolith. *The Moon*, 13 (1–3), 339–353. https://doi.org/10.1007/BF00567525

Head, J.W., & Gifford, A. (1980). Lunar Mare Domes: Classification and Modes of Origin. *The Moon and the Planets*, 22 (2), 235. https://doi.org/10.1007/BF00898434

Heiken, G., Vaniman, D., & French, B.M. (1991). *Lunar Source Book*. New York: Cambridge University Press, 357-474.

Ketkar, N. (2017). *Introduction to keras*. In Deep learning with Python. Apress, Berkeley, CA, 97-111.

Kingma, D. P., Ba, J. (2014). Adam: A method for stochastic optimization. *arXiv preprint arXiv*, 1412.6980.

https://doi.org/10.48550/arXiv.1412.6980

Jia, B., Fa, W., Xie, M., Tai, Y., & Liu, X. (2021). Regolith properties in the Chang'E-5 landing region of the Moon: Results from multi-source remote sensing observations. *J. Geophys. Res., Planets*, 126, e2021JE006934. https://doi.org/10.1029/2021JE006934

Jia, B., Fa, W., Zhang, M., Di, K., Xie, M., Tai, Y., & Li, Y. (2022). On the provenance of the Chang'E-5 lunar samples. *Earth Planet. Sci. Lett*, 596, 117791. https://doi.org/10.1016/j.epsl.2022.117791

Jolliff, B.L., Gillis, J.J., Haskin, L.A., et al. (2000). Major lunar crustal terranes: surface expressions and crust-mantle origins. *J. Geophys. Res.: Planets*, 105 (E2), 4197–4216. https://doi.org/10.1029/1999JE001103

Lemelin, M., Lucey, P.G., Song, E., & Taylor, G.J. (2015). Lunar central peak mineralogy and iron content using the Kaguya multiband imager: reassessment of the compositional structure of the LUNAR crust: LUNAR CENTRAL PEAK MINERALOGY AND IRON. *J. Geophys. Res.: Planets*, 120 (5), 869–887. https://doi.org/10.1002/2014JE004778

Lemelin, M., Lucey, P. G., Gaddis, L.R., Hare, T., & Ohtake, M. (2016). *Global map products from the Kaguya Multiband Imager at 512 ppd: Minerals, FeO and OMAT*. Paper presented at 43 rd Lunar and Planetary Science Conference (abs. #2994).

Li, C., Hu, H., Yang, M., Pei, Z., Zhou, Q., Ren, X., et al. (2022). Characteristics of the lunar samples returned by the Chang'E-5 mission. *National Science Review*, 9(2), nwab188. https://doi.org/10.1093/nsr/nwab188

Li, Q. L., et al. (2021). Two-billion-year-old volcanism on the Moon from Chang'e-5 basalts. *Nature*, 600,54-58. https://doi.org/10.1038/s41586-021-04100-2

Liebermann, R.C., & Ringwood, A.E. (1976). Elastic properties of anorthite and the nature of the lunar crust. *Earth Planet. Sci. Lett*, 31 (1), 69–74. https://doi.org/10.1016/0012-821X(76)90097-2

Ling, Z. C., Zhang, J., Liu, J. Z., et al. (2010). Preliminary results of FeO mapping from Chang'E-1 IIM data (in Chinese). *Chinese Sci Bull*, 55(35), 3373-3377.

Ling, Z.C., Zhang, J., Liu, J.Z., et al. (2011). Preliminary results of TiO_2 mapping using imaging interferometer data from Chang'E-1 (in Chinese). *Chinese. Sci. Bull*, 56(16), 1257–1263.

Ling, Z., Jolliff, B. L., Wang, A., Li, C., Liu, J., Zhang, J., et al. (2015). Correlated compositional and mineralogical investigations at the Chang e-3 landing site. *Nature Communications*, 6(1), 1–9. https://doi.org/10.1038/ncomms9880

Lecun, Y., Bottou, Y., et al. (1998). Gradient-based learning applied to document recognition. *Proc. IEEE*, 86 (11): 2278–2324.

Lu, Y., Wu, Y. Z., Li, C., et al. (2021). Seamless maps of major elements of the Moon: Results from high-resolution geostationary satellite. *Research in Astronomy and Astrophysics*, 21(2), 031.

https://doi.org/10.1088/1674-4527/21/2/31

Lucey, P.G., Taylor, G.J., & Malaret, E. (1995). Abundance and distribution of iron on the Moon. *Science*, 268 (5214), 1150–1153. https://doi.org/10.1126/science.268.5214.1150

Lucey, P.G., Blewett, D.T., & Hawke, B.R. (1998). Mapping the FeO and TiO_2 content of the lunar surface with multispectral imagery. *J. Geophys. Res*, 103(E2), 3679. https://doi.org/10.1029/97JE03019

Lucey, P.G., Blewett, D.T., & Jolliff, B.L. (2000). Lunar iron and titanium abundance algorithms based on final processing of Clementine ultraviolet-visible images. *J. Geophys. Res*, 105 (E8), 20297. https://doi.org/10.1029/1999JE001117

Ma, M., Li, B., Chen, S., et al. (2021). Global estimates of lunar surface chemistry derived from LRO diviner data. *Icarus*, 371(4020), 114697. https://doi.org/10.1016/j.icarus.2021.114697

Malek, S., Melgani, F., & Bazi, Y. (2018). One- dimensional convolutional neural networks for spectroscopic signal regression. *Journal of Chemometrics*,

32 (e2977). https://doi.org/10.1002/cem.2977

Ohtake, M., Haruyama, J., et al. (2008). Performance and scientific objectives of the SELENE (KAGUYA) Multiband Imager. *Earth Planets & Space*, 60(4), 257-264. https://doi.org/10.1186/BF03352789

Ohtake, M., Pieters, C.M., Isaacson, P.J., Besse, S., Yokota, Y., Matsunaga, T., Boardman, J., Yamomoto, S., Haruyama, J., & Staid, M. (2013). One Moon, many measurements 3: spectral reflectance. *Icarus*, 226 (1), 364–374. https://doi.org/10.1016/j.icarus.2013.05.010

Otake, H., Ohtake, M., & Hirata, N. (2012). *Lunar iron and titanium abundance algorithms based on SELENE (kaguya) multiband imager data*. Paper presented at 43 rd Lunar and Planetary Science Conference (abs. #1905).

Papike, J.J. (1988). Chemistry of the rock-forming silicates: Multiple-chain, sheet, and framework structures. *Rev. Geophys*, 26 (3), 407–444. https://doi.org/10.1029/RG026i003p00407

Pieters, C.M., Taylor, L.A., Noble, S.K., Keller, L.P., Hapke, B., Morris, R.V., et al. (2000). Space weathering on airless bodies: resolving a mystery with lunar samples. *Meteorit. Planet. Sci*, 35 (5), 1101–1107. https://doi.org/10.1111/j.1945-5100.2000.tb01496.x

Prettyman, T.H., Hagerty, J.J., Elphic, R.C., et al. (2006). Elemental composition of the lunar surface: analysis of gamma ray spectroscopy data from lunar prospector. *J. Geophys. Res.: Planets*, 111 (E12). https://doi.org/10.1029/2005JE002656

Qian, Y., Xiao, L., Head, J. W., van der Bogert, C. H., Hiesinger, H., & Wilson, L. (2021a). Young lunar mare basalts in the Chang'e-5 sample return region, northern Oceanus Procellarum. *Earth Planet. Sci. Lett*, 555, 116702. https://doi.org/10.1016/j.epsl.2020.116702

Qian, Y., Xiao, L., Wang, Q., Head, J. W., Yang, R., Kang, Y., vander Bogert, C. H., Hiesinger, H., Lai, X., Wang, G., Pang, Y., Zhang, N., Yuan, Y., He, Q., Huang, J., Zhao, J., Wang, J., & Zhao, S. (2021b). China's Chang'e-5 landing site: Geology, stratigraphy, and provenance of materials. *Earth Planet. Sci. Lett*, 561, 116855. https://doi.org/10.1016/j.epsl.2021.116855

Qiao, L., Head, J.W., Xiao, L., Wilson, L., & Dufek, J.D. (2018). The role of substrate characteristics in producing anomalously young crater retention ages in volcanic deposits on the Moon: Morphology, topography, subresolution roughness and mode of emplacement of the Sosigenes lunar irregular mare patch. *Meteoritics & Planetary Science*, 53(4), 778. https://doi.org/10.1111/maps.13003

Qiao, L., Head, J. W., Ling, Z., & Wilson, L. (2020). Lunar Irregular Mare Patches: Classification, Characteristics, Geologic Settings, Updated Catalog, Origin, and Outstanding Questions. *Journal of Geophysical Research: Planets*, 125 (7). https://doi.org/10.1029/2019JE006362

Qiu, D., Li, F., J, Yan., et al. (2021). Machine learning for inversing FeO and TiO_2 content on the Moon: Method and comparison. *Icarus*, 373. https://doi.org/10.1016/j.icarus.2021.114778

Sato, H., Robinson, M.S., Lawrence, S.J., Denevi, B.W., Hapke, B., Jolliff, B.L., & Hiesinger, H. (2017). Lunar mare TiO_2 abundances estimated from UV/Vis reflectance. *Icarus*, 296, 216–238. https://doi.org/10.1016/j.icarus.2017.06.013

Stooke, P. (2012). *Lunar meniscus hollows*. Paper presented at Lunar and Planetary Science Conference, (abs. #1011).

Sun, L., Ling, Z., Zhang, J., Li, B., Chen, J., Wu, Z., & Liu, J. (2016). Lunar iron and optical maturity mapping: results from partial least squares modeling of Chang'E-1 IIM data. *Icarus*, 280, 183–198. https://doi.org/10.1016/j.icarus.2016.07.010

Surkov, Y., Shkuratov, Y., Kaydash, V., Korokhin, V., & Videen, G. (2020). Lunar ilmenite content as assessed by improved Chandrayaan-1 M3 data. *Icarus*, 341, 113661. https://doi.org/10.1016/j.icarus.2020.113661

Taylor, G. J., Warren, P., Ryder, G., et al. (1991). *Lunar Sourcebook*. Cambridge: Cambridge University Press, 183–284.

Taylor, S.R. (1987). The unique lunar composition and its bearing on the origin of the Moon. *Geochim. Cosmochim. Acta*, 51(5), 1297-1309. https://doi.org/10.1016/0016-7037(87)90220-1

Taylor, S.R., Taylor, G.J., & Taylor, L.A. (2006). The moon: a Taylor perspective. *Geochim.Cosmochim. Acta*, 70 (24), 5904–5918. https://doi.org/10.1016/j.gca.2006.06.262

Tian, H.C., Wang, H., Chen, Y., et al. (2021). Non-KREEP origin for Chang'e-5 basalts in the Procellarum KREEP Terrane. *Nature*, 600, 7887. https://doi.org/10.1038/s41586-021-04119-5

Vulova, S., Meier, F., Rocha, A.D., Quanz, J., Nouri, H., & Kleinschmit, B. (2021). Modeling urban evapotranspiration using remote sensing, flux footprints, and artificial intelligence. *Sci. Total Environ*, 786, 147293. https://doi.org/10.1016/j.scitotenv.2021.147293

Wang, X., Zhang, J., & Ren, H. (2021). Lunar surface chemistry observed by the KAGUYA multiband imager. *Planetary and Space Science*, 209, 105360. https://doi.org/10.1016/j.pss.2021.105360

Wilcox, B.B., Lucey, P.G., & Gillis, J. J. (2005). Mapping iron in the lunar mare: An improved approach. *J Geophys Res*, 110(E11). https://doi.org/10.1029/2005JE00251

Wu, Y., (2012). Major elements and mg# of the moon: results from Chang'E-1 interference imaging spectrometer (IIM) data. *Geochim. Cosmochim. Acta*, 93, 214–234. https://doi.org/10.1016/j.gca.2012.07.011

Xia, W., Wang, X., Zhao, S., Jin, H., Chen, X., Yang, M., et al. (2019). New maps of lunar surface chemistry. *Icarus*, 321, 200–215. https://doi.org/10.1016/j.icarus.2018.10.031

Yan, B., Xiong, S.Q., Wu, Y., et al. (2012). Mapping lunar global chemical composition from Chang'E-1 IIM data. *Planetary Space Sci*, 67 (1), 119–129. https://doi.org/10.1016/j.pss.2012.03.010

Yuan, Q., Wang, J., Zheng, M., et al. (2022). Hybrid 1D-CNN and attention-based Bi-GRU neural networks for predicting moisture content of sand gravel using NIR spectroscopy. *Construction and Building Materials*, 350: 128799. https://doi.org/10.1016/j.conbuildmat.2022.128799

Zhang, J., Yang, W., Hu, S., et al. (2015). *Volcanic history of the imbrium basin: a close-up view from the lunar rover yutu.* Proceedings of the National Academy of Sciences of the United States of America 112(17), 5342-7.

Zhuang, F., Qi, Z., Duan, K., Xi, D., Zhu, Y., Zhu, H., et al. (2020). A comprehensive survey on transfer learning. *Proc. IEEE*, 109 (1), 43–76.

Zong K., et al. (2022). Bulk compositions of the Chang'E-5 lunar soil: Insights into chemical homogeneity, exotic addition, and origin of landing site basalts. *Geochim. Cosmochim. Acta*, 335, 284-296. https://doi.org/10.1016/j.gca.2022.06.037

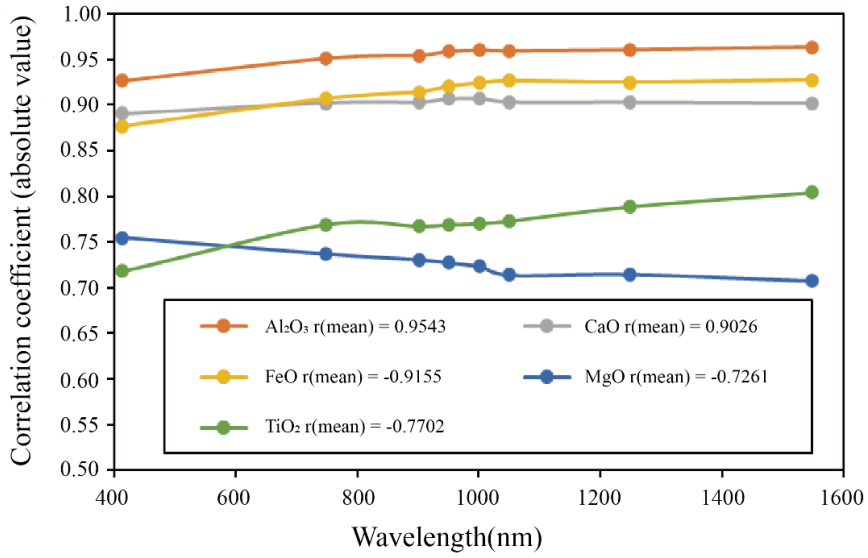

Figure 1. Absolute values of Pearson correlation coefficient between five major

oxide contents and MI reflection value. Where, positive correlation (Al_2O_3, CaO) and negative correlation (FeO, MgO, TiO_2). The correlation coefficient was calculated from 40 lunar sampling points. The r (mean) represents the average value of the Pearson correlation coefficient in all bands.

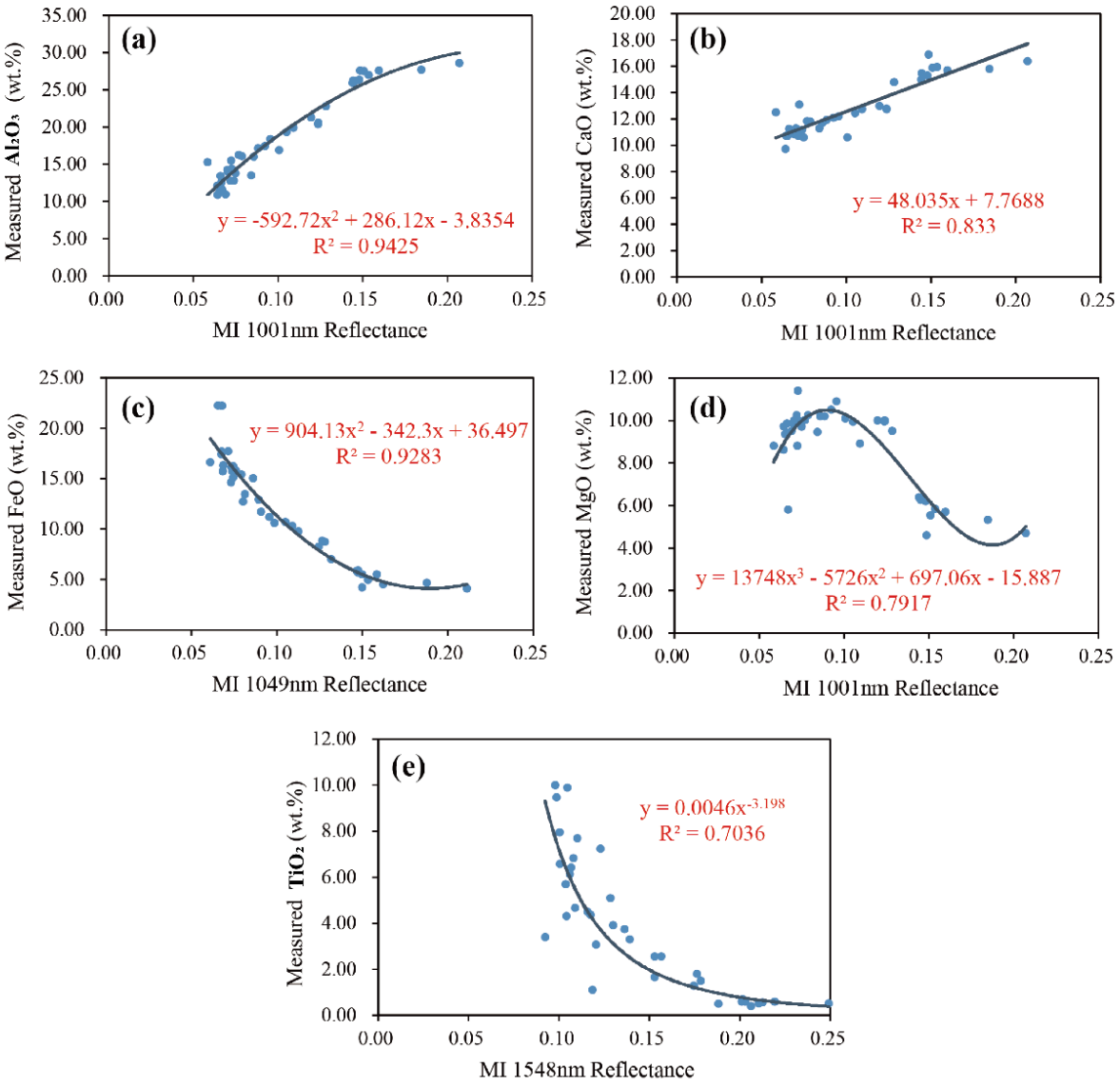

Figure 2. Linear or nonlinear relations between (a) Al_2O_3, (b) CaO, (c) FeO, (d) MgO, and(e) TiO_2 contents and the reflectance values of one MI band. Only (b) is linear, and (a), (c), (d), and (e) are nonlinear.

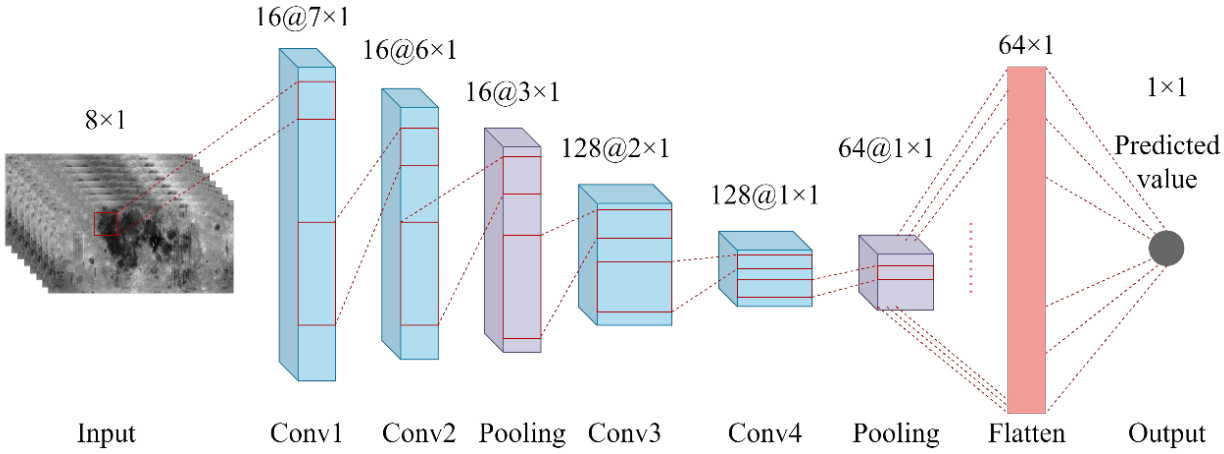

Figure 3. Regression model of lunar major oxides based on 1D-CNN. The input layer of the network is the average spectral data of lunar sampling points with the size of 1×8. The size of convolution kernel used in convolution operation is 1×2. After the Conv1, 16 characteristic maps of 1×7 size are output; after the Conv2, 16 characteristic maps of 1×6 size are output; after down sampling, the Pooling layer outputs characteristic maps of 1×3 size; after the Conv3, 128 characteristic maps of 1×2 size are output; after the Conv4, 128 characteristic maps of 1×1 size are output; after the Pooling layer, 64 characteristic maps of 1×1 size are output; the Flatten layer pulls these characteristic maps to a vector of 1×64 size. Finally, the predicted value is output through the output layer.

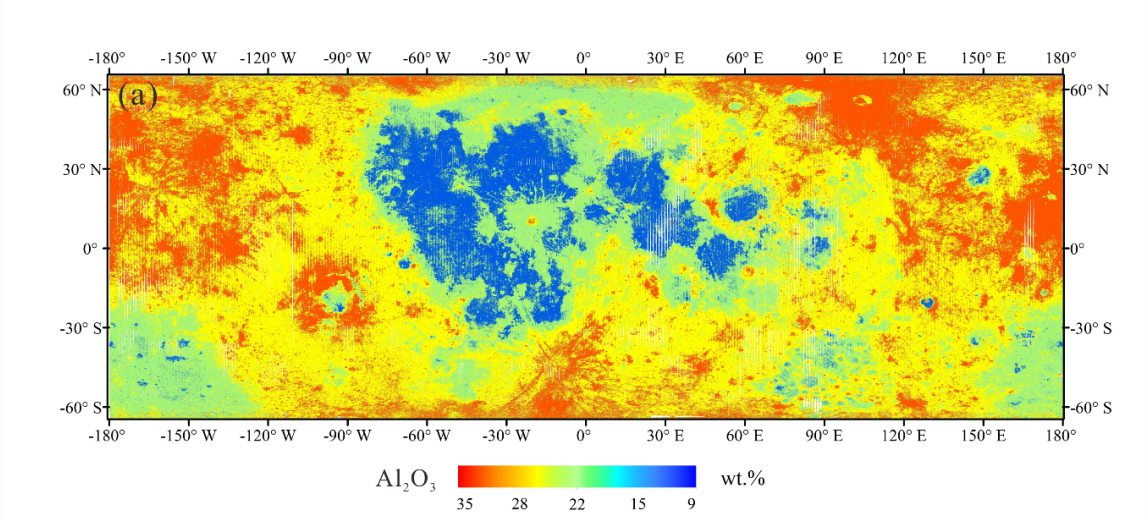

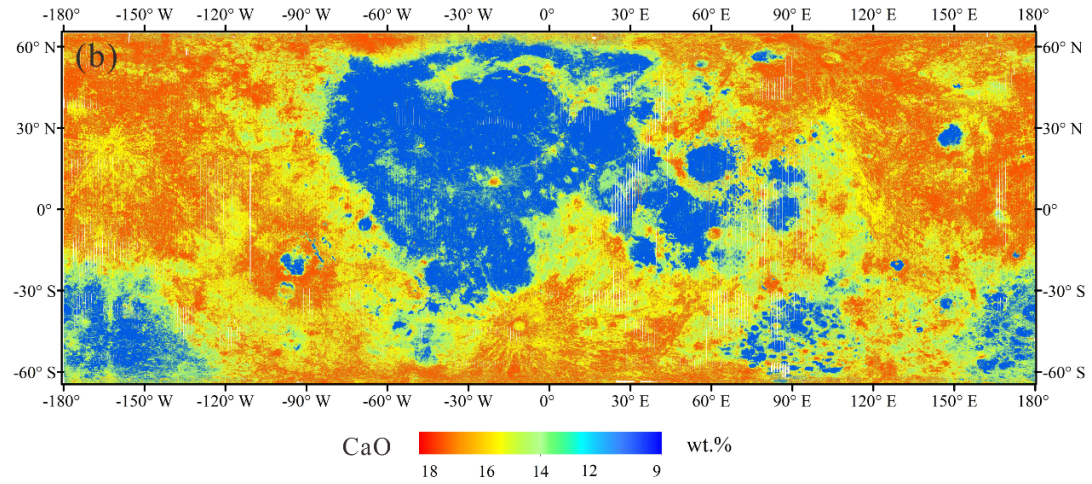
(b)
-180° -150° W -120° W -90° W -60° W -30° W 0° 30° E 60° E 90° E 120° E 150° E 180°
60° N
30° N
0°
-30° S
-60° S
CaO
wt.%
18 16 14 12 9

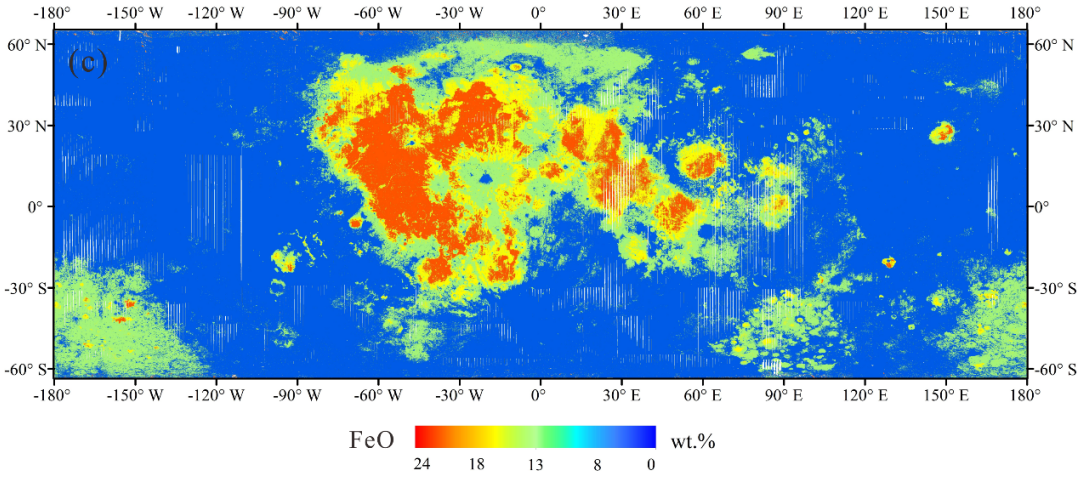
(c)
-180° -150° W -120° W -90° W -60° W -30° W 0° 30° E 60° E 90° E 120° E 150° E 180°
60° N
30° N
0°
-30° S
-60° S
FeO
wt.%
24 18 13 8 0

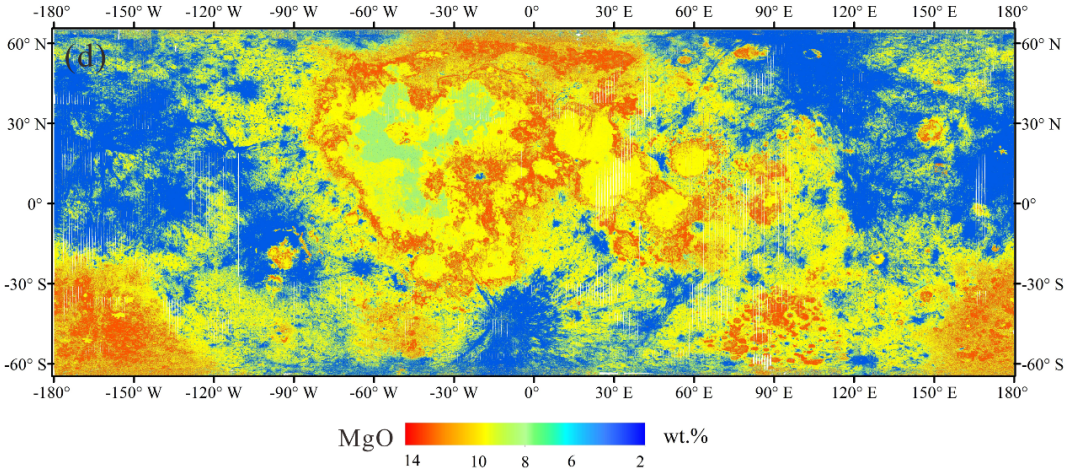
(d)
-180° -150° W -120° W -90° W -60° W -30° W 0° 30° E 60° E 90° E 120° E 150° E 180°
60° N
30° N
0°
-30° S
-60° S
MgO
14 10 8 6 2
wt.%

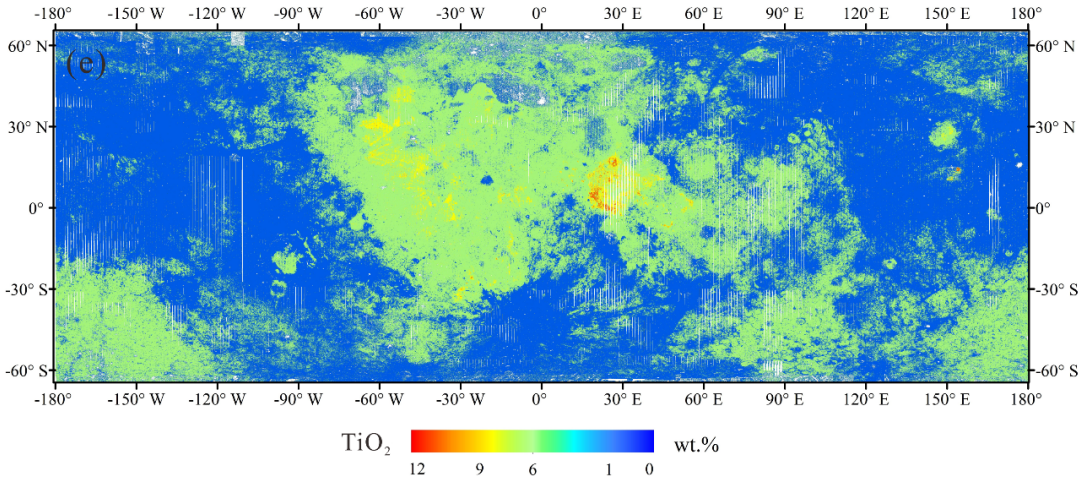
(c)
-180° -150° W -120° W -90° W -60° W -30° W 0° 30° E 60° E 90° E 120° E 150° E 180°
60° N
30° N
0°
-30° S
-60° S
TiO2
12 9 6 1 0
wt.%

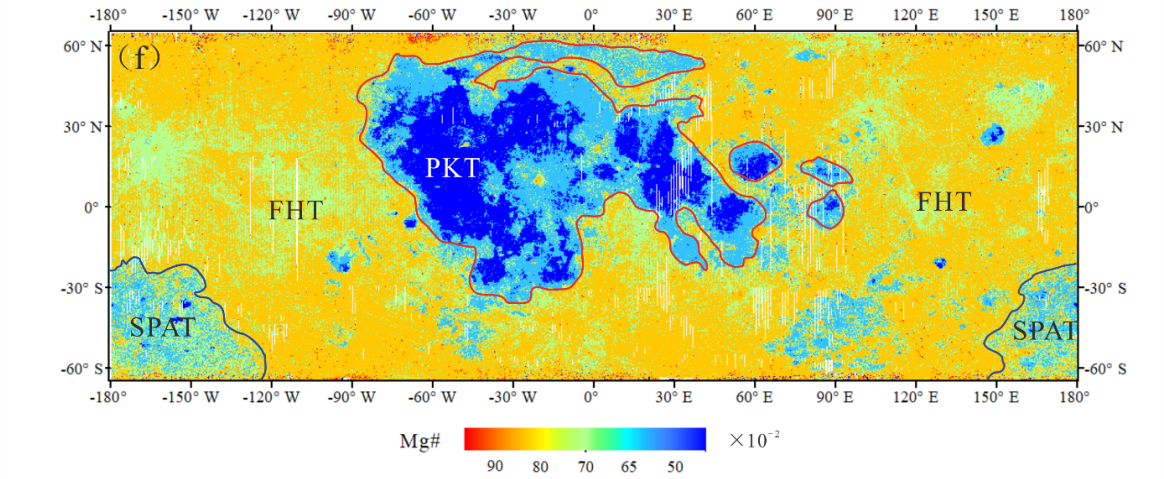

Figure 4. Maps of (a) Al_2O_3; (b) CaO; (c) FeO; (d) MgO; (e) TiO_2 abundances and (f) Mg #. The Mg # map highlights the approximate boundaries of three lunar geological terranes (PKT, FHT, and SPAT) (Jolliff et al., 2000). The red lines mark the PKT unit, the blue lines encircle the SPAT unit, and the remaining region is the FHT unit.

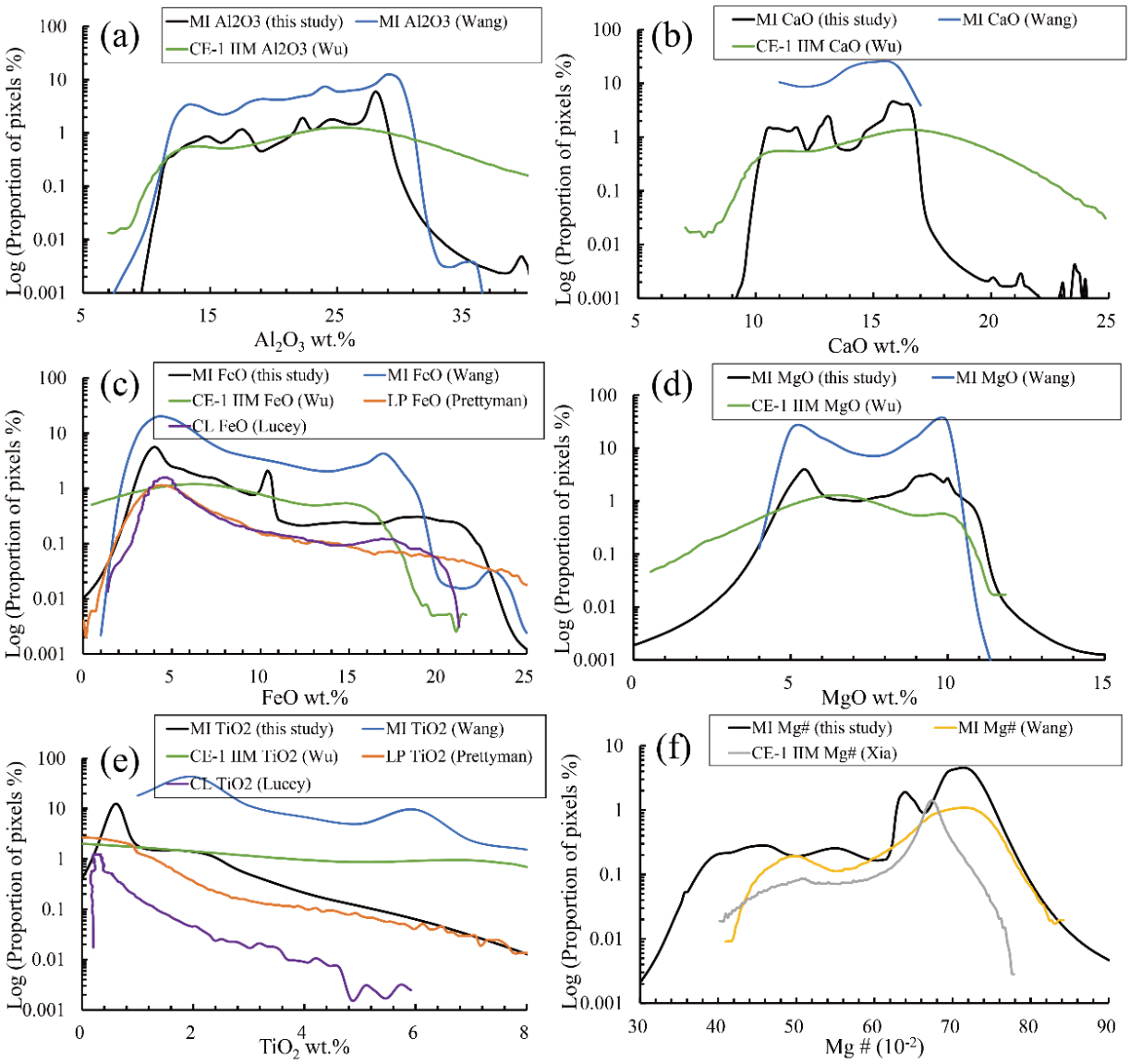

Figure 5. Histograms of (a) Al_2O_3; (b) CaO; (c) FeO; (d) MgO; (e) TiO_2 and (f) Mg # for the lunar surface. The ordinate is the Log value of the percentage of pixels with a certain abundance in the total number of pixels. The black line is the result of this study; the blue line is the histograms of elemental abundances derived from MI data (Wang et al., 2021); the green line is the histograms of elemental abundances derived from IIM data (Wu, 2012); the orange line is the histograms of FeO and TiO_2 abundances derived from LP GNRS data (Prettyman et al., 2006); the purple line is the histograms of FeO and TiO_2

abundances derived from Clementine data (Lucey at al., 1998); the yellow line is the histograms of Mg # derived from MI data (Wang et al., 2021); the gray line is the histograms of Mg # derived from IIM data (Xia et al., 2019).

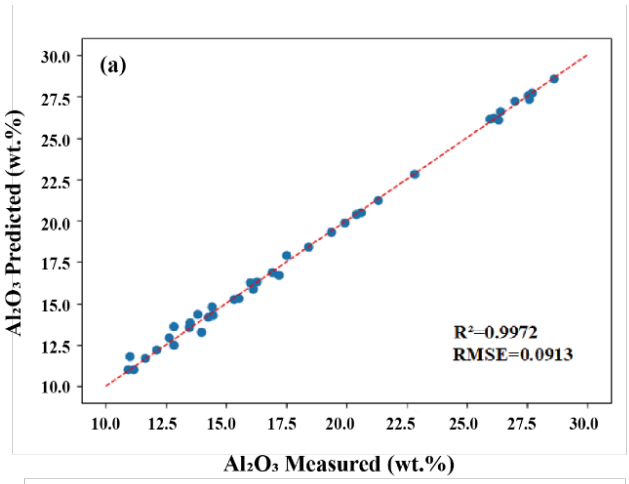
(a)
R²=0.9972
RMSE=0.0913
Al₂O₃ Predicted (wt.%)
Al₂O₃ Measured (wt.%)

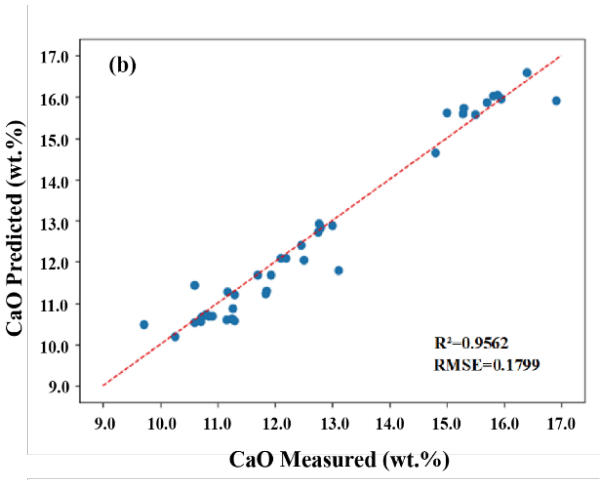
(b)
R²=0.9562
RMSE=0.1799
CaO Predicted (wt.%)
CaO Measured (wt.%)

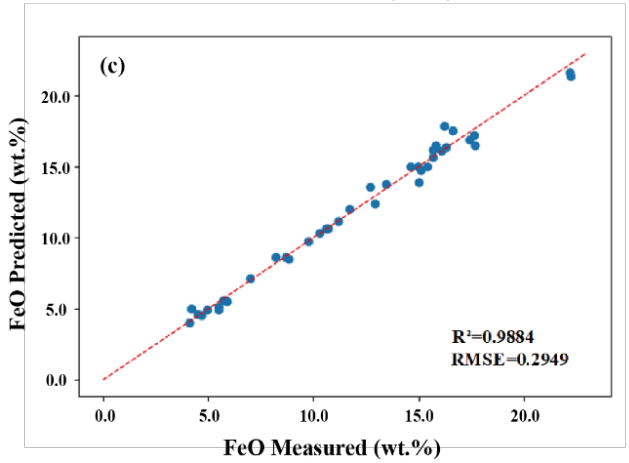
(c)
R²=0.9884
RMSE=0.2949
FeO Predicted (wt.%)
FeO Measured (wt.%)

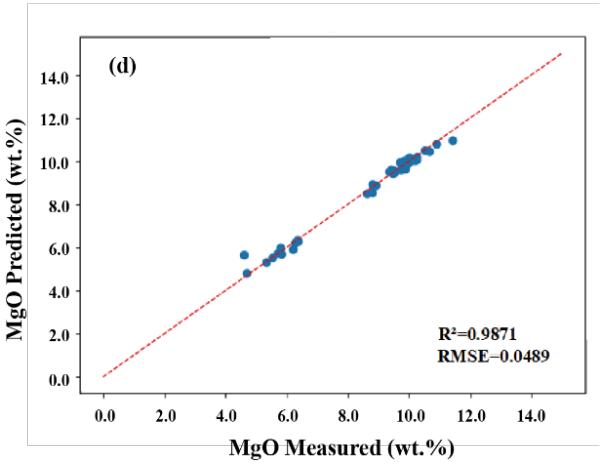
(d)
R²=0.9871
RMSE=0.0489
MgO Predicted (wt.%)
MgO Measured (wt.%)

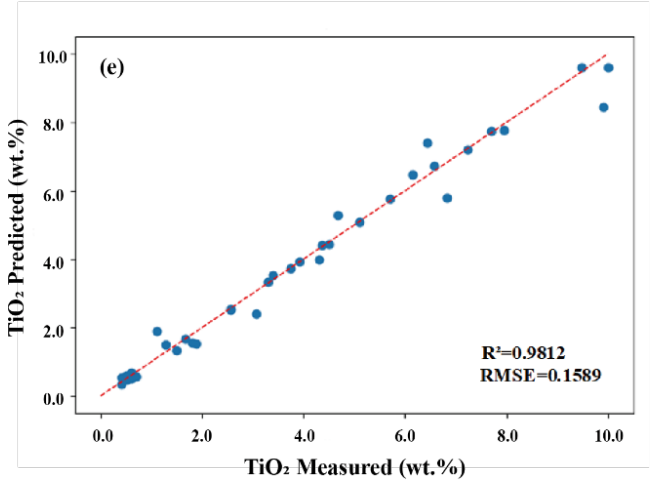
(e)
R²=0.9812
RMSE=0.1589
TiO₂ Predicted (wt.%)
TiO₂ Measured (wt.%)

Figure 6. Scatter plots of the measured and predicted values for CNN model for (a) Al_2O_3, (b) CaO, (c) FeO, (d) MgO, and (e) TiO_2.

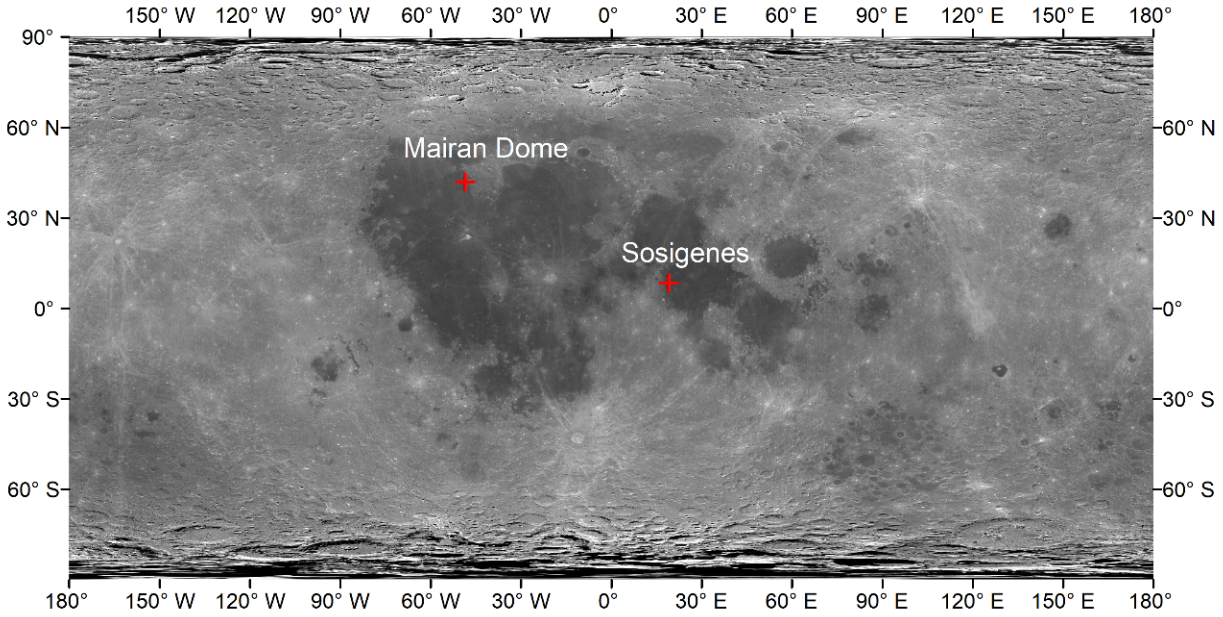

Figure 7. Location map of the region of interest includes Mairan Dome (43.76°N, 49.90°W) and Sosigenes (8.34°N, 19.07°E). The background is CE-1 Digital Orthophoto Map (DOM) of 120 m/pixel.

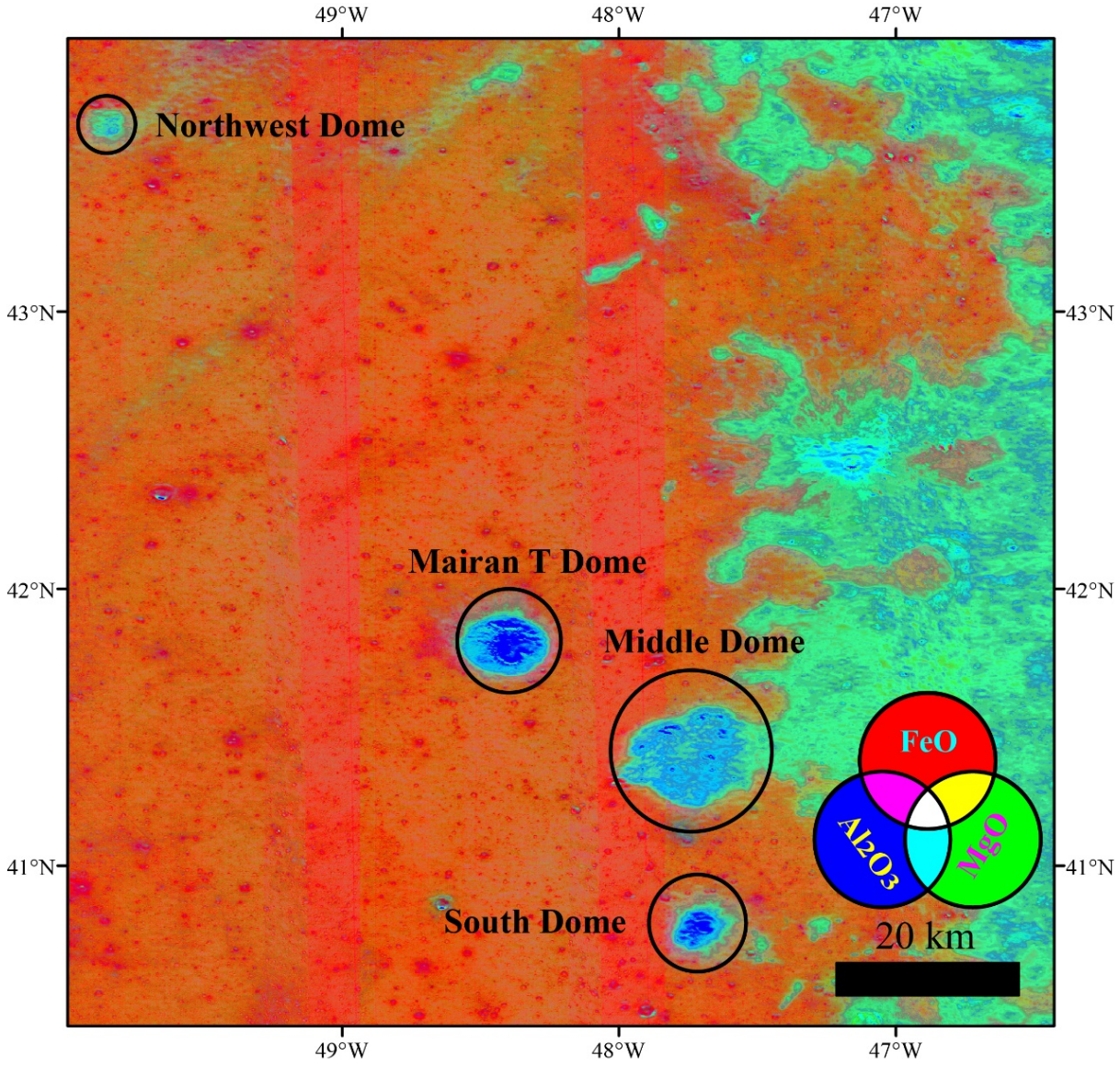

Figure 8. Color composite image of Mairan Domes. The red channel is FeO abundance (stretched from 0.50 to 31.10). The Green channel is MgO abundance (stretched from 1.48 to 13.81). The blue channel is Al_2O_3 abundance (stretched from 9.17 to 32.50). Black lines correspond to the boundaries of the domes as determined from the oxides content and the digital elevation model (DEM) based on Lunar Orbiter Laser Altimeter (LOLA) on board the Lunar Reconnaissance Orbiter mission (LRO).

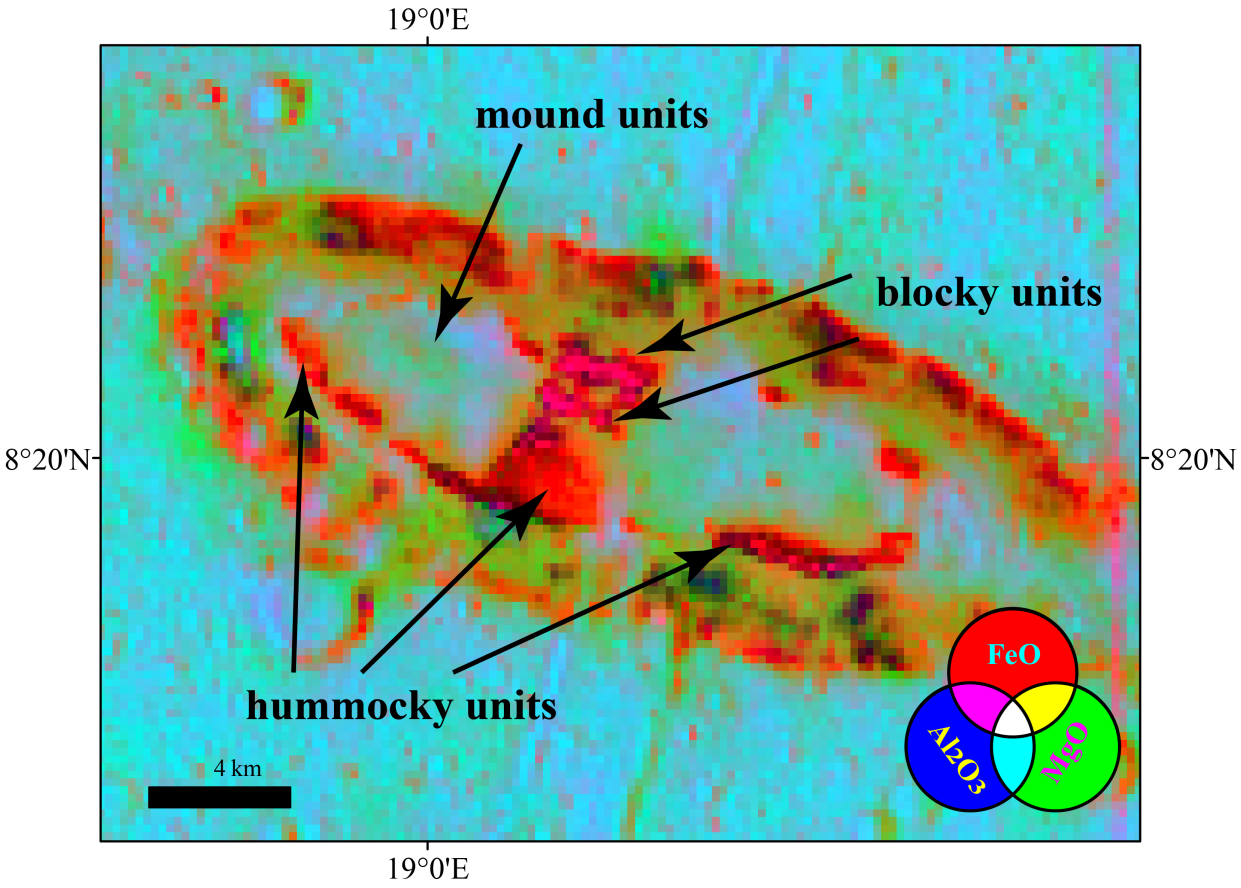

Figure 9. Color composite image of Sosigenes. The red channel is FeO abundance (stretched from 15.50 to 25.58). The Green channel is MgO abundance (4.31 to 9.43). The blue channel is Al_2O_3 abundance (7.52 to 17.12). The green line indicates the identified Mound units; the blue line indicates the identified Hummocky units; the red line indicates the identified Blocky units.

Table 1. Contents of chemical components at sampling points of monthly surface oxides.

Site	Al_2O_3 wt.%	CaO wt.%	FeO wt.%	MgO wt.%	TiO_2 wt.%
Apollo12LM					
Apollo14LM					
Apollo15LM					
Apollo16LM					
Apollo16S1					
Apollo16S2					
Apollo16S4					

Site	Al_2O_3 wt.%	CaO wt.%	FeO wt.%	MgO wt.%	TiO_2 wt.%
Apollo16S5					
Apollo16S6					
Apollo16S8					
Apollo16S9					
Apollo16S11					
Apollo16S13					
Apollo17LM					
Apollo17S1					
Apollo17S2					
Apollo17S3					
Apollo17S4					
Apollo17S5					
Apollo17S6					
Apollo17S7					
Apollo17S8					
Apollo17S9					
Apollo17LRV1					
Apollo17LRV2					
Apollo17LRV3					
Apollo17LRV4					
Apollo17LRV5					
Apollo17LRV6					
Apollo17LRV7					
Apollo17LRV8					
Apollo17LRV9					
Apollo17LRV10					
Apollo17LRV11					
Apollo17LRV12					
Luna16					
Luna20					
Luna24					
CE-3					
CE-5					

Table 2. Means of five oxide abundances of the moon.

	Al_2O_3 (wt.%)	CaO (wt.%)	FeO (wt.%)	MgO (wt.%)	TiO_2 (wt.%)
This study					
Global					
Mare					
Highland					

	Al_2O_3 (wt.%)	CaO (wt.%)	FeO (wt.%)	MgO (wt.%)	TiO_2 (wt.%)
Global (Wu, 2012)					
Global (Wang et al., 2021)					

Table 3. The predicted values for the five oxides of the 1D-CNN model

Site	Al_2O_3 wt.%	CaO (wt.%)	FeO (wt.%)	MgO (wt.%)	TiO_2 (wt.%)
Apollo12LM					
Apollo14LM					
Apollo15LM					
Apollo16LM					
Apollo16S1					
Apollo16S2					
Apollo16S4					
Apollo16S5					
Apollo16S6					
Apollo16S8					
Apollo16S9					
Apollo16S11					
Apollo16S13					
Apollo17LM					
Apollo17S1					
Apollo17S2					
Apollo17S3					
Apollo17S4					
Apollo17S5					
Apollo17S6					
Apollo17S7					
Apollo17S8					
Apollo17S9					
Apollo17LRV1					
Apollo17LRV2					
Apollo17LRV3					
Apollo17LRV4					
Apollo17LRV5					
Apollo17LRV6					
Apollo17LRV7					
Apollo17LRV8					
Apollo17LRV9					

Site	Al_2O_3 wt.%	CaO (wt.%)	FeO (wt.%)	MgO (wt.%)	TiO_2 (wt.%)
Apollo17LRV10					
Apollo17LRV11					
Apollo17LRV12					
Luna16					
Luna20					
Luna24					
Chang'E 3					
Chang'E 5					

Table 4. Comparison of five major oxide abundances derived from this work with Wang et al. (2021) and Xia et al. (2019) models.

	Al_2O_3 wt%	CaO (wt%)	FeO (wt%)	MgO (wt%)	TiO_2 (wt%)
This work					
R^2					
RMSE					
Wang et al. (2021)					
R^2					
RMSE					
Xia et al. (2019)					
R^2					
RMSE					

Table 5. Five elements content of the Mairan Domes.

	MgO wt%	Al_2O_3 wt%	CaO wt%	TiO_2 wt%	FeO wt%
Northeast					
Mairan T					
Middle					
South					
mare					
highlands					

Table 6. Five elements content of Sosigenes.

	MgO wt%	Al_2O_3 wt%	CaO wt%	TiO_2 wt%	FeO wt%
Mound units					
Hummocky units					
Blocky units					
mare					